Solar-Terrestrial Physics. 2023. Vol. 9. Iss. 3. P. 30–42. DOI: 10.12737/stp-93202305. © 2023
O.I. Akhmetov, I.V. Mingalev, O.V. Mingalev, V.B. Belakhovsky, E.A. Maurchev, A.V. Larchenko, Z.V. Suvorova, Yu.V. Balabin. Published by INFRA-M Academic Publishing House

UDC 537,877, 519.6
DOI: 10.12737/stp-93202305

Received November 02, 2023
Accepted June 27, 2023

INFLUENCE OF STRONG SOLAR PROTON EVENTS ON PROPAGATION OF RADIO SIGNALS IN THE VLF RANGE IN A HIGH-LATITUDE REGION

O.I. Akhmetov
Polar Geophysical Institute, Apatity, Russia, akhmetov@pgia.ru

I.V. Mingalev
Polar Geophysical Institute, Apatity, Russia, mingalev_i@pgia.ru

O.V. Mingalev
Polar Geophysical Institute, Apatity, Russia, mingalev_o@pgia.ru
Murmansk Arctic State University, Murmansk, Russia

V.B. Belakhovsky
Polar Geophysical Institute, Apatity, Russia, belakhovsky@pgia.ru

E.A. Maurchev
Polar Geophysical Institute, Apatity, Russia, maurchev@pgia.ru

A.V. Larchenko
Polar Geophysical Institute, Apatity, Russia, alexey.larchenko@gmail.com

Z.V. Suvorova
Polar Geophysical Institute, Apatity, Russia, suvorova@pgia.ru

Yu.V. Balabin
Polar Geophysical Institute, Apatity, Russia, balabin@pgia.ru

Abstract. In this paper, we examine the features of RSDN-20 signal propagation in a high-latitude Earth–ionosphere waveguide during solar proton events, using computational experiment methods. We have analyzed two proton ground-level enhancement (GLE) events of December 13, 2006 (GLE70) and September 10, 2017 (GLE72). Electron density profiles were constructed using the Global Dynamic Model of Ionosphere (GDMI) and the RUSCOSMICS model, developed at PGI. We present estimated phase and amplitude changes in RSDN-20 signals during precipitation of high-energy protons in the high-latitude region of the Earth–ionosphere waveguide. From the results of computational experiments and the analysis of the electromagnetic signal attenuation based on analytical Maxwell's equation system solution in magnetized ionospheric plasma, we have found a pattern in the signal attenuation frequency dependence associated simultaneously with the signal reflection height, electron density profiles, and the collision frequency of electrons with neutral particles and ions. We discuss limitations of the computational experiment method and compare simulation results with data from Lovozero and Tuloma observatories.

Keywords: numerical modeling, radio wave propagation, ionosphere, high latitudes, GLE, VLF, RSDN-20, GDMI.

INTRODUCTION

Solar proton events (SPEs) are ejections of very high-energy particles (MeV–GeV) from the Sun's surface, which are driven by solar flares. Most (90 %) high-energy particles are protons, the remaining part includes helium nuclei and elements with Z>2, as well as electrons with positrons. Solar proton events that cause an increase in the count rate of ground-based neutron monitors are called Ground Level Enhancement (GLE) events [Meyer et al., 1956]. Such events are quite rare: only 73 GLE events have been observed on record. SPEs lead to an increase in radiation levels in near-Earth orbit and at aircraft altitudes.

Penetration of solar protons into Earth's atmosphere causes the electron density in the lower layers of the ionosphere (D-region) to increase; therefore, the quality of radio communications, radar, and radio navigation can significantly deteriorate in polar regions. For example, Knipp et al. [2016] have shown that the absorption of American radar signals caused by SPE in May 1967 almost caused a nuclear war between the United States and the USSR. The ionospheric response to penetration of solar protons as absorption of radio waves (10–50 MHz) was called polar cap absorption (PCA).

Clilverd et al. [2006] using a receiver on the Svalbard archipelago have detected significant absorption of very low-frequency (VLF) signals during a SPE event in October–November 2003. There were also noticeable VLF signal amplitude fluctuations.

In the recent past, VLF signals were widely used all over the world to provide long-distance communication and navigation. The VLF band (3–30 kHz) is well suited for such tasks due to the effective locking of a signal in the Earth–ionosphere waveguide. In an undisturbed ionosphere, this allows VLF signals to propagate with low attenuation (about 2–3 dB/Mm) [Marshall et al., 2017]. Currently, ground-based long-range navigation and communication systems using VLF signals have been supplanted by satellite data transmission and navigation systems, yet some of the VLF transmitters are still active. Their signals can be employed for sounding the D-region [Inan et al., 2010; Dowden, Adams, 1989]: since the dominant source of signal change for a static path is a change in the ionosphere, transmitted signal amplitude

and phase measurements facilitate direct measurement of the ionospheric variability. In such studies, it is important to understand the relationship between signal variations and the changes in the ionosphere that cause the variations.

Over the past few years, the Polar Geophysical Institute (PGI) has been using numerical simulation to study the influence of ionospheric conditions on propagation of infra- and very low-frequency signals in the high-latitude region of the Earth–ionosphere waveguide. Akhmetov et al. [2019] have analyzed signals with a frequency of 1500 Hz. Then, signals with frequencies corresponding to the frequencies of signals from the RSDN-20 long-range navigation radio system (11, 12, 14 kHz) [Akhmetov et al., 2021a] and the frequencies of signals from the Beta exact time system (20, 23 kHz) [Akhmetov et al., 2021b] were examined. The above works allow a conclusion that among the signals considered the RSDN-20 signals are most strongly affected by density variations in the D layer.

In this paper, we present estimated RSDN-20 signal phase and amplitude variations during precipitation of high-energy protons in the high-latitude region of the Earth–ionosphere waveguide. We discuss changes in signal amplitude attenuation caused by GLE events depending on their frequency and height of reflection from the ionosphere. We compare the results obtained in computational experiments with the results of observations made at the PGI observatories Lovozero and Tuloma.

1. EVENTS OF INTEREST

GLE70, the last event of solar cycle 23, occurred on December 13, 2006 at 02:40 UT. The active region A930 with coordinates S06W24 produced an X3.4/2B solar flare, which was accompanied by type II, IV radio bursts and a halo-type coronal mass ejection. As recorded by neutron monitors, the event lasted for ~5 hrs. While GLE70 occurred during the descending phase of the cycle, it was quite a powerful event (the third most intense in cycle 23). The greatest increase in cosmic ray intensity was observed at the Oulu station (92 %). The fact that the maximum intensity was not detected by polar stations suggests that the source of cosmic ray anisotropy was near the ecliptic plane [Mishev, Velinov, 2015].

During cycle 24, only two proton events were recorded — GLE71 (May 17, 2012) and GLE72 (September 10, 2017). GLE72 was initiated by an X8.2 flare with coordinates S08W83, started at 15:35 UT, peaked at 16:06 UT. The GLE72 amplitude as measured by neutron monitors (NMs) of the global network did not exceed 6 % according to 5-min data [Perez-Peraza et al., 2020].

2. MODELS EMPLOYED

Propagation of RSDN-20 signals has been calculated using an electromagnetic signal propagation model developed at PGI. It is based on numerical integration of a system of Maxwell's equations together with the equation closing this system (the linearized equation of electron motion in the atmosphere and ionosphere), and Ohm's law in the lithosphere [Akhmetov et al., 2023].

The ionosphere, atmosphere, and lithosphere in the model are considered horizontally homogeneous. The vertical profile of the rate of ionization q, generated by high-energy protons penetrating into the high-latitude atmosphere, has been calculated using the RUSCOSMICS model developed at PGI. We have determined the primary spectrum of solar cosmic rays from the worldwide ground-based neutron monitor network's data by the method of solving the inverse problem and from GOES data by a unique technique developed with the participation of co-authors of this paper [Maurchev, Balabin, 2016].

For GLE70, the solar cosmic ray spectrum was divided into Prompt Component (PC) and Delay Component (DC). PC is observed during the amplitude increase phase, it is characterized by strong anisotropy and exponential spectrum. DC usually appears near the maximum and is then observed until the end of the event; it features moderate anisotropy and exponential spectrum [Maurchev, Balabin, 2016].

The electron density profiles for quiet conditions and for conditions with GLE have been calculated using the Global Dynamic Model of Ionosphere (GDMI) [Shubin, 2017; Deminov et al., 2021; Shubin et al., 2021].

The geomagnetic field for experiments corresponding to the coordinates of Apatity and Barentsburg and the dates of GLEs have been calculated by the 13th generation IGRF model [Alken et al., 2021].

The vertical conductivity profile of the lithosphere was given by the model presented in [Korja et al., 2002].

3. ELECTRON DENSITY PROFILES DENSITY CALCULATIONS

Electron density profiles are shown in Figure1: GLE70 and GLE72 in Apatity (*a*, *b*); GLE72 in Barentsburg (*c*).

The electron density profiles for quiet conditions at altitudes above 60 km have been calculated by the GDMI model. Near the Earth surface, the density was assumed to be $N_{e\_0}=10^2$ m^{-3}; from $h_0=0$ km to a minimum height h_{GDMI}, it was interpolated by a power-law dependence $N_{e\_0\text{-}GDMI} = N_{e\_0}{}^{(1-X)} N_{e\_GDMI}{}^{X}$; $X = \left(h_0 / h_{GDMI}\right)^2$. We have not use the parametric profile proposed in [Wait, Spies, 1964] and developed by other scientists because if such a profile is combined with the GDMI model profile, the electron density in the troposphere is lower than 1 m^{-3}.

The electron density profile for disturbed conditions has been found by adding an electron density, caused by penetration of high-energy solar protons during GLE, to the profile for quiet conditions. The additional density was recovered from the ionization rate profiles obtained by the RUSCOSMICS model. The additional electron density $n_e(h)$ during SPE was calculated by the well-known formula $n_e(h) = \sqrt{q(h)/\alpha(h)}$ [Hargreaves, 1979], where $q(h)$ is the ionization rate, and $\alpha(h)$ is the effective recombination coefficient [cm^3 s^{-1}]. According to the empirical dependence obtained by Gledhill [1986] from experimental data for heights 50–100 km, $\alpha(h) = 0.501\exp(-0.165\,h)$, where h is the height [km].

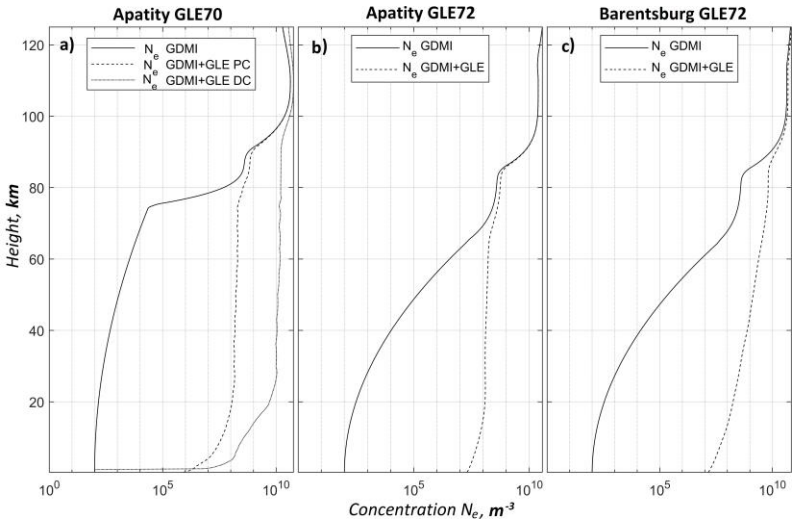

Figure 1. Vertical electron density profiles: Apatity, GLE 70, December 13, 2006, 04:00 UTC (*a*); Apatity, GLE 72, September 10, 2017, 16:15 UTC (*b*); Barentsburg, GLE 72, September 10, 2017, 16:15 UTC (*c*)

The model spectrum of cosmic ray protons in the RUSCOSMICS model for GLE70 contains prompt (PC) and decay (DC) components that differ in energy spectrum and are separated by time (Figure 1, *a*). For GLE72, the cosmic ray proton spectrum was not divided into the two components (Figure 1, *b*, *c*).

The profiles of frequency of collisions of electrons with neutrals and ions were calculated from electron density profiles and NRLMSISE2000 model data, using formulas on page 109 of the book [Schunk, Nagy, 2009].

Numerical calculations were carried out in a Cartesian coordinate system with the Z-axis pointing vertically upward. Thus, the modeling region for numerical experiments was a parallelepiped, including a segment of the Earth–ionosphere waveguide. The level of the Earth surface corresponded to the plane $\{z = 0\}$.

Numerical experiments used a horizontally homogeneous ionosphere and a region 256×1000 km in horizon, 125 km in height in the atmosphere and ionosphere, and 25 km in depth in the lithosphere. The grid spacing vertically above the Earth surface Δz=0.25 km, in the lithosphere Δz=0.125 km, and horizontally Δx=Δy=0.5 km. The center of the signal source was at a distance of 64 km from three lateral faces of the resulting parallelepiped.

The source signal was a sum of sinusoids at RSDN-20 signal frequencies of 11905, 12679, and 14881 Hz. At a distance of 64 km from the left vertical boundary of the rectangular modeling region on a part of the vertical plane 128 km wide parallel to this boundary at altitudes to 60 km from the Earth surface, we set a horizontal magnetic field of an RSDN-20 signal. This allowed us to define a plane wavefront in the first approximation.

4. ANALYSIS OF RESULTS OF COMPUTATIONAL EXPERIMENTS

The paper has analyzed two GLE events in terms of propagation of RSDN-20 VLF signals in a high-latitude region. Analysis of amplitudes of magnetic and electric components of an electromagnetic signal and its propagation velocity during the arrival of DC of the strong GLE70 event has shown an increase in signal attenuation more than five times and a noticeable decrease in its propagation velocity, which cause phase errors (Tables 1 and 2). Presumably, during strong GLE events at high latitudes, the use of the RSDN-20 system as intended might be impossible. At the same time, such significant amplitude and phase variations can be a good indicator of the electron density profile on a high-latitude radio path. The weaker GLE72 event and PC of the GLE70 event also have a noticeable effect on RSDN-20 signals (see Tables 1 and 2) — it is likely that the range of confident reception will decrease and positioning errors will increase if a receiver is located at high latitudes.

Figure 2 plots signal Pointing vector attenuation as function of frequency on the Earth surface as a percentage per 1 km of radio path during GLE70 (Apatity, panel *a*) and GLE72 (Barentsburg and Apatity, panels *b*, *c*).

Table 1 and Figure 2 show that under quiet conditions and with a relatively weakly disturbed ionosphere for GLE72 in Apatity the decrease in the signal Pointing vector at 12679 Hz is noticeably greater than at 11905 and 14881 Hz, i.e. the frequency dependence of attenuation is nonmonotonic. In the case of a strongly disturbed ionosphere for GLE70 in Apatity, a linear decrease in attenuation with frequency is observed. In the case of a moderately disturbed ionosphere for GLE72 in Barentsburg, this dependence decreases monotonically, yet it is not linear.

A violation of the monotonicity of the signal attenuation dependence on its frequency is associated with peculiarities of radio wave propagation in magnetized collisional and highly inhomogeneous ionospheric plasma and can be explained as follows.

In the high-latitude ionosphere, where the geomagnetic field is nearly vertical, for signals whose electric field is also nearly vertical there are two height regions with significantly different signal attenuation modes.

Table 1

RSDN-20 signal attenuation expressed in terms of 1 km of radio path

Computational experiment	Pointing vector attenuation, %/km	*E* attenuation, %/km	*H* attenuation, %/km
Apatity, GLE70, December 13, 2006, 04:00 UTC			
GDMI 11905 Hz	0.294	0.15	0.157
GDMI 12649 Hz	0.420	0.224	0.232
GDMI 14881 Hz	0.364	0.196	0.192
GDMI + GLE PC 11905 Hz	0.649	0.365	0.364
GDMI + GLE PC 12649 Hz	0.66	0.372	0.371
GDMI + GLE PC 14881 Hz	0.569	0.314	0.314
GDMI + GLE DC 11905 Hz	1.408	1.01	1.01
GDMI + GLE DC 12649 Hz	1.385	0.982	0.981
GDMI + GLE DC 14881 Hz	1.287	0.874	0.873
Barentsburg, GLE72, September 10, 2017, 16:15 UTC			
GDMI 11905 Hz	0.283	0.149	0.143
GDMI 12649 Hz	0.321	0.169	0.165
GDMI 14881 Hz	0.27	0.142	0.14
GDMI + GLE 11905 Hz	0.786	0.456	0.456
GDMI + GLE 12649 Hz	0.779	0.452	0.451
GDMI + GLE 14881 Hz	0.674	0.38	0.38
Apatity, GLE72, September 10, 2017, 16:15 UTC			
GDMI 11905 Hz	0.252	0.132	0.124
GDMI 12649 Hz	0.295	0.155	0.149
GDMI 14881 Hz	0.268	0.141	0.14
GDMI + GLE 11905 Hz	0.568	0.314	0.313
GDMI + GLE 12649 Hz	0.586	0.325	0.324
GDMI + GLE 14881 Hz	0.502	0.273	0.272

Disturbed conditions are marked in gray.

Table 2

RSDN-20 signal phase delay expressed in terms of 1 km of radio path relative to propagation in vacuum

Computational experiment	Energy flux phase delay, rad/km	Phase delay *E*, rad/km	Phase delay *H*, rad/km
Apatity, GLE70, December 13, 2006, 04:00 UTC			
GDMI 11905 Hz	0.0096	0.018	0.0169
GDMI 12649 Hz	0.0051	0.0089	0.0079
GDMI 14881 Hz	0.0082	0.0087	0.0085
GDMI + GLE PC 11905 Hz	0.0083	0.0141	0.0134
GDMI + GLE PC 12649 Hz	0.0062	0.0082	0.0079
GDMI + GLE PC 14881 Hz	0.0087	0.009	0.008
GDMI + GLE DC 11905 Hz	0.1229	0.0755	0.0738
GDMI + GLE DC 12649 Hz	0.0827	0.0537	0.0521
GDMI + GLE DC 14881 Hz	0.0239	0.0151	0.0159
Barentsburg, GLE72, September 10, 2017, 16:15 UTC			
GDMI 11905 Hz	0.0145	0.0214	0.021
GDMI 12649 Hz	0.0115	0.0189	0.0181
GDMI 14881 Hz	0.0077	0.0106	0.0104
GDMI + GLE 11905 Hz	0.0122	0.0183	0.0168
GDMI + GLE 12649 Hz	0.0091	0.0102	0.011
GDMI + GLE 14881 Hz	0.0074	0.0081	0.0084
Apatity, GLE72, September 10, 2017, 16:15 UTC			
GDMI 11905 Hz	0.0157	0.0244	0.0222
GDMI 12649 Hz	0.0129	0.0183	0.0185
GDMI 14881 Hz	0.0075	0.0108	0.0107
GDMI + GLE 11905 Hz	0.0075	0.015	0.0149
GDMI + GLE 12649 Hz	0.0055	0.0092	0.009
GDMI + GLE 14881 Hz	0.009	0.0082	0.0078

Disturbed conditions are marked in gray.

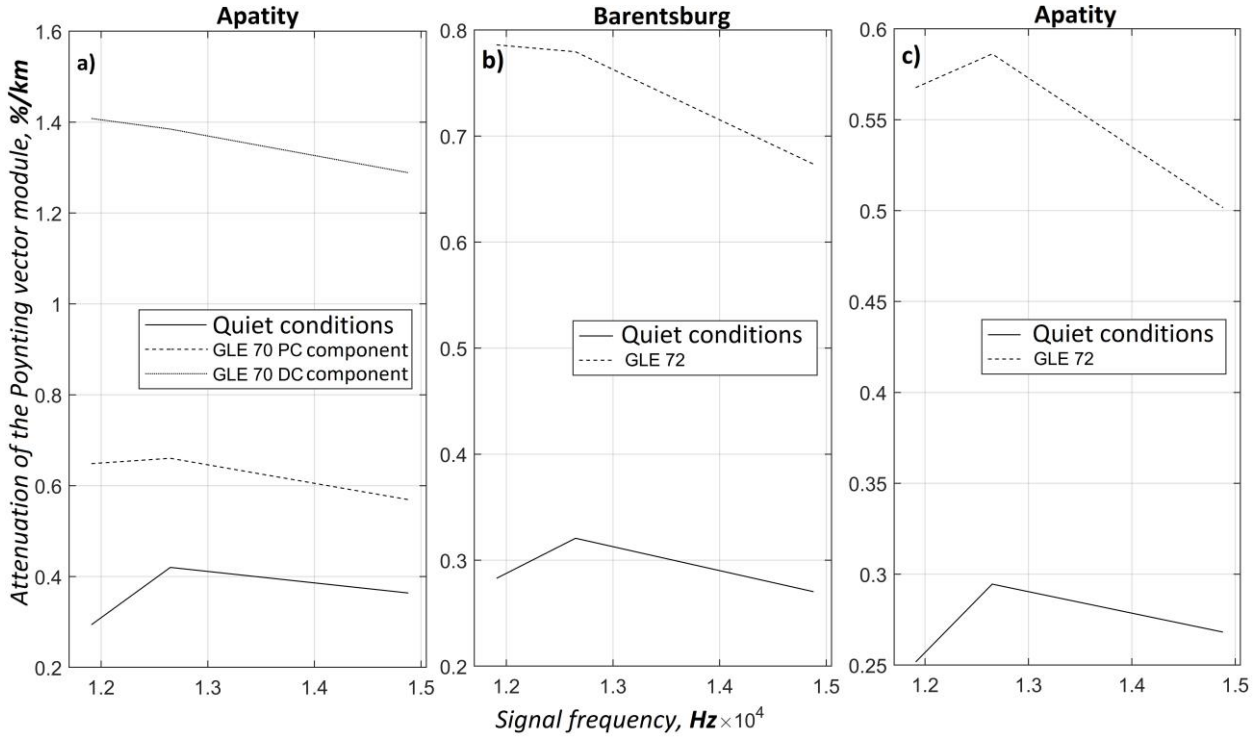

Figure 2. Energy loss as a percentage per 1 km of radio path as function of frequency at ground level: Apatity, GLE 70, December 13, 2006, 04:00 UTC (*a*); Barentsburg, GLE 72, September 10, 2017, 16:15 UTC (*b*); Apatity, GLE 72, 10 September 2017, 16:15 UTC *c*

The boundary between these regions is a surface that is approximately described by the equation

$$\nu_e(\mathbf{r}) = 2\omega_{pe}(\mathbf{r}),$$

where $\nu_e(\mathbf{r})$ is the frequency of collisions of electrons with neutral atoms and ions (decreases with increasing height); $\omega_{pe}(\mathbf{r}) = e\sqrt{n_e(\mathbf{r})/(\varepsilon_0 m_e)}$ is the plasma frequency in the SI system (increases with increasing height); $n_e(\mathbf{r})$ is the electron density. Below this boundary is a region in which the condition $\nu_e(\mathbf{r}) > 2\omega_{pe}(\mathbf{r})$ is met and one attenuation mode of a weak signal takes place; above it is a region in which $\nu_e(\mathbf{r}) < 2\omega_{pe}(\mathbf{r})$, hence another attenuation mode of a weak signal takes place.

Under quiet conditions, signals of the three frequencies in the ionosphere over Apatity and Barentsburg are reflected in a layer ~15 km thick, which approximately covers in half the top of the lower region (determined by $\nu_e > 2\omega_{pe}$) and the bottom of the upper region (defined by $\nu_e < 2\omega_{pe}$). Under disturbed conditions due to the increased electron density in the ionosphere, the signal reflection layer is significantly shifted downward and lies completely in the lower region determined by $\nu_e > 2\omega_{pe}$. This explains the different signal attenuation in quiet and disturbed conditions.

To substantiate these statements, we examine the process of signal attenuation at the upper boundary of the Earth–ionosphere waveguide in the case of closure of the system of Maxwell's equations by the linearized equation of momentum flux for electrons in a collisional plasma in the presence of the external magnetic field, which is traditionally used to describe propagation of weak signals in the Earth–ionosphere waveguide.

Let us introduce the following notations: $\mathbf{r}=(x, y, z)$ is the vector of Cartesian coordinates in space $\mathbb{R}^3$; t is time; $\mathbf{E}(\mathbf{r}, t)$, $\mathbf{D}(\mathbf{r}, t)$, $\mathbf{H}(\mathbf{r}, t)$, $\mathbf{D}(\mathbf{r}, t)$ are the vectors of intensity and induction of signal electric and magnetic fields; $\mathbf{j}(\mathbf{r}, t)$ is the signal current density; $\mathbf{B}_0(\mathbf{r})$ is the induction vector of a given external geomagnetic field; $B_0(\mathbf{r}) = |\mathbf{B}_0(\mathbf{r})|$ and $\mathbf{b}_0(\mathbf{r}) = \mathbf{B}_0(\mathbf{r})/B_0(\mathbf{r})$ is its magnitude and the unit vector along it. For an arbitrary vector field $\mathbf{a}(\mathbf{r}, t)$, we introduce its longitudinal $a_\parallel(\mathbf{r}, t)$ and orthogonal $a_\perp(\mathbf{r}, t)$ components, as well as longitudinal $\mathbf{a}_\parallel(\mathbf{r}, t)$ and $\mathbf{a}_\perp(\mathbf{r}, t)$ parts with respect to the external geomagnetic field, which are found from the formulas

$$a_\parallel = (\mathbf{a}\mathbf{b}_0),\ \mathbf{a}_\parallel = a_\parallel \mathbf{b}_0,\ \mathbf{a}_\perp = \mathbf{a} - \mathbf{a}_\parallel. \quad (1)$$

Maxwell's equations for induction in the case of plasma have the same form as in vacuum [Lifshits, Pitaevsky, 1979], and in the SI system take the form

$$\mathrm{div}\mathbf{B} = 0,\ \frac{\partial \mathbf{B}}{\partial t} = -\mathrm{rot}\mathbf{E},\ \mathrm{div}\mathbf{D} = 0,\ \frac{\partial \mathbf{D}}{\partial t} = \mathrm{rot}\mathbf{H}. \quad (2)$$

In plasma, the material equations [Lifshits, Pitaevsky, 1979] in the SI system have the form

$$\mathbf{B}(\mathbf{r}, t) = \mu_0 \mathbf{H}(\mathbf{r}, t),$$
$$\mathbf{D}(\mathbf{r}, t) = \varepsilon_0 \mathbf{E}(\mathbf{r}, t) + \mathbf{P}(\mathbf{r}, t),$$

where ε_0 and μ_0 are the electric and magnetic constants; $\mathbf{P}(\mathbf{r}, t)$ is the polarization vector related to the plasma current density $\mathbf{j}(\mathbf{r}, t)$ and its charge density $\rho(\mathbf{r}, t)$ by the relations

$$\operatorname{div}\mathbf{P}(\mathbf{r},t)=-\rho(\mathbf{r},t),$$
$$\frac{\partial\mathbf{P}(\mathbf{r},t)}{\partial t}=\mathbf{j}(\mathbf{r},t).$$

We deal with sufficiently high-frequency signals with frequencies by orders of magnitude higher than the cyclotron frequency of ions, with a low amplitude, and a wavelength by orders of magnitude greater than the Debye radius of electrons in the ionosphere. For such signals, it can be assumed that the signal current density is created only by electrons, i.e. $\mathbf{j}\equiv\mathbf{j}_e$. System of Maxwell's equations (2) is closed by the linearized equation of momentum flux for electrons, written in terms of the density of their current produced by the signal field:

$$\begin{aligned}&\frac{\partial\mathbf{j}(\mathbf{r},t)}{\partial t}=\nu_e(\mathbf{r})\mathbf{j}(\mathbf{r},t)+\omega_{ce}(\mathbf{r})\times\\&\times\left[\mathbf{b}_0(\mathbf{r})\times\mathbf{j}(\mathbf{r},t)\right]+\varepsilon_0\omega_{pe}^2(\mathbf{r})\mathbf{E}(\mathbf{r},t),\end{aligned}\tag{3}$$

where $\omega_{ce}(\mathbf{r})=eB_0(\mathbf{r})/m_e$ is the gyrofrequency of electrons in the external geomagnetic field. As a result, the system of equations that determines the signal field and is numerically solved in the model will take the form

$$\begin{aligned}&\frac{\partial\mathbf{B}}{\partial t}=-\mathrm{rot}\mathbf{E};\ \frac{\partial\mathbf{E}}{\partial t}=c_0^2\mathrm{rot}\mathbf{B}-\frac{1}{\varepsilon_0}\mathbf{j},\\&\frac{\partial\mathbf{j}}{\partial t}=-\nu_e\mathbf{j}+\omega_{ce}\left[\mathbf{b}_0\times\mathbf{j}\right]+\varepsilon_0\omega_{pe}^2\mathbf{E},\end{aligned}\tag{4}$$

where $c_0=1/\sqrt{\varepsilon_0\mu_0}$ is the speed of light in vacuum.

To analyze signal attenuation, we can drop spatial derivatives in equations (4) since they describe spatial signal propagation. As a result, we have a system of linear ordinary differential equations with first-order time derivatives and the coordinate **r** as a parameter:

$$\begin{aligned}&\frac{\partial\mathbf{E}}{\partial t}=-\frac{1}{\varepsilon_0}\mathbf{j},\\&\frac{\partial\mathbf{j}}{\partial t}=-\nu_e\mathbf{j}+\omega_{ce}\left[\mathbf{b}_0\times\mathbf{j}\right]+\varepsilon_0\omega_{pe}^2\mathbf{E}.\end{aligned}\tag{5}$$

Substituting the first equation in (5) into the second yields a linear homogeneous system of second-order differential (in time *t*) equations with respect to the electric field **E**(**r**, *t*):

$$\begin{aligned}&\frac{\partial^2\mathbf{E}(\mathbf{r},t)}{\partial t^2}+\nu_e(\mathbf{r})\frac{\partial\mathbf{E}(\mathbf{r},t)}{\partial t}-\\&-\omega_{ce}(\mathbf{r})\left[\mathbf{b}_0(\mathbf{r})\times\frac{\partial\mathbf{E}(\mathbf{r},t)}{\partial t}\right]+\omega_{pe}^2(\mathbf{r})\mathbf{E}(\mathbf{r},t)=0.\end{aligned}\tag{6}$$

For system of equations (6), we can obtain an analytical solution of the Cauchy problem with the initial condition

$$\mathbf{E}(\mathbf{r},t^0)=\mathbf{E}^0(\mathbf{r}),\ \mathbf{j}(\mathbf{r},t^0)=\mathbf{j}^0(\mathbf{r}).\tag{7}$$

To derive the analytical solution, it is necessary to divide Cauchy problem (6), (7) into two independent problems for longitudinal and orthogonal parts of the electric field. Apply decomposition (1) into longitudinal and transverse parts to **E**(**r**, *t*) and **j**(**r**, *t*):

$$\begin{aligned}&\mathbf{E}(\mathbf{r},t)=E_{\parallel}(\mathbf{r},t)\mathbf{b}_0(\mathbf{r})+\mathbf{E}_{\perp}(\mathbf{r},t),\\&\mathbf{j}(\mathbf{r},t)=j_{\parallel}(\mathbf{r},t)\mathbf{b}_0(\mathbf{r})+\mathbf{j}_{\perp}(r,t).\end{aligned}\tag{8}$$

Substituting expressions (8) into equations (5) and (6), as well as into initial condition (7), gives Cauchy problems for the longitudinal part of the electric field:

$$\begin{aligned}&\frac{\partial^2E_{\parallel}(\mathbf{r},t)}{\partial t^2}+\nu_e(\mathbf{r})\frac{\partial E_{\parallel}(\mathbf{r},t)}{\partial t}+\\&+\omega_{pe}^2(\mathbf{r})E_{\parallel}(\mathbf{r},t)=0,\end{aligned}\tag{9}$$

$$\mathbf{j}_{\parallel}=-\varepsilon_0\frac{\partial E_{\parallel}}{\partial t},$$

$$E_{\parallel}(\mathbf{r},t^0)=E_{\parallel}^0(\mathbf{r}),\ j_{\parallel}(\mathbf{r},t^0)=j_{\parallel}^0(\mathbf{r}),\tag{10}$$

and also for its orthogonal part:

$$\begin{aligned}&\frac{\partial\mathbf{E}_{\perp}}{\partial t^2}+\nu^2(\mathbf{r})\frac{\partial\mathbf{E}_{\perp}}{\partial t}-\omega_{ce}(\mathbf{r})\left[\mathbf{b}_0(\mathbf{r})\times\frac{\partial\mathbf{E}_{\perp}}{\partial t}\right]+\\&+\omega_{pe}^2(\mathbf{r})\mathbf{E}_{\perp}=\mathbf{0},\end{aligned}\tag{11}$$

$$j_{\perp}=-\varepsilon_0\frac{\partial E_{\perp}}{\partial t},$$

$$\mathbf{E}_{\perp}(\mathbf{r},t^0)=\mathbf{E}_{\perp}^0(\mathbf{r}),\ \mathbf{j}_{\perp}(\mathbf{r},t^0)=\mathbf{j}_{\perp}^0(\mathbf{r}).\tag{12}$$

The first equation in (9) for $E_{\parallel}(\mathbf{r},t)$ at each fixed **r** is the well-known equation of harmonic oscillator with attenuation, which has the standard form

$$\frac{d^2x(t)}{dt^2}+2\gamma_0\frac{dx(t)}{dt}+\omega_0^2x(t)=0,$$

where the $\gamma_0=\nu_e(\mathbf{r})/2$, $\omega_0=\omega_{pe}(\mathbf{r})$. Solution of Cauchy problem (9), (10) for longitudinal components depends on the sign of function

$$Q(\mathbf{r})=\nu_e^2(\mathbf{r})-4\omega_{pe}^2(\mathbf{r})\tag{13}$$

and is given by the following formulas, which use the notations $\tau=t-t^0$ and

$$q(\mathbf{r})=\sqrt{|Q(\mathbf{r})|}=\sqrt{|\nu_e^2(\mathbf{r})-4\omega_{pe}^2(\mathbf{r})|}:$$

for $Q(\mathbf{r})>0$, i.e. when $\nu_e(\mathbf{r})>2\omega_{pe}(\mathbf{r})$,

$$\begin{aligned}&E_{\parallel}(\mathbf{r},t)=\exp\left(-\frac{\nu_e\tau}{2}\right)\times\\&\times\left(E_{\parallel}^0\left(\mathrm{ch}\left(\frac{q\tau}{2}\right)+\frac{\nu_e}{q}\mathrm{sh}\left(\frac{q\tau}{2}\right)\right)-\frac{2j_{\parallel}^0}{\varepsilon_0 q}\mathrm{sh}\left(\frac{q\tau}{2}\right)\right);\end{aligned}\tag{14}$$

for $Q(\mathbf{r})=0$, i.e. when $\nu_e(\mathbf{r})=2\omega_{pe}(\mathbf{r})$,

$$\begin{aligned}&E_{\parallel}(\mathbf{r},t)=\exp\left(-\frac{\nu_e(\mathbf{r})\tau}{2}\right)\times\\&\times\left(E_{\parallel}^0(\mathbf{r})\left(1+\frac{\nu_e(\mathbf{r})\tau}{2}\right)-\frac{1}{\varepsilon_0}j_{\parallel}^0(\mathbf{r})\tau\right);\end{aligned}\tag{15}$$

for $Q(\mathbf{r}) < 0$, i.e. when $\nu_e(\mathbf{r}) < 2\omega_{pe}(\mathbf{r})$,

$$E_{\parallel}(\mathbf{r}, t) = \exp\left(-\frac{\nu_e \tau}{2}\right) \times \times \left(E_{\parallel}^0 \left(\cos\left(\frac{q\tau}{2}\right) + \frac{\nu_e}{q} \sin\left(\frac{q\tau}{2}\right) \right) - \frac{2 j_{\parallel}^0}{\varepsilon_0 q} \sin\left(\frac{q\tau}{2}\right) \right). \quad (16)$$

Note that solution (14) for the lower region decays exponentially with time as

$$\exp\left(-\frac{\tau}{2}\left(\nu_e(\mathbf{r}) - q(\mathbf{r})\right)\right) = = \exp\left(-\frac{\tau}{2}\left(\nu_e(\mathbf{r}) - \sqrt{\nu_e^2(\mathbf{r}) - 4\omega_{pe}^2(\mathbf{r})}\right)\right),$$

and solution (16) for the upper region decays with time as $\exp\left(-\frac{\tau}{2}\nu_e(\mathbf{r})\right)$, i.e. much faster.

The analytical solution of Cauchy problem (11), (12) for orthogonal components does not depend on the sign of function (13), i.e. it is the same for both $\nu_e(\mathbf{r}) > 2\omega_{pe}(\mathbf{r})$ and $\nu_e(\mathbf{r}) < 2\omega_{pe}(\mathbf{r})$. This solution has a form similar to (16) and a rather cumbersome linear combination of four terms as a product of a damped exponent and a harmonic function

$$\exp(-\alpha_1\tau)\cos(\omega_1\tau), \quad \exp(-\alpha_1\tau)\sin(\omega_1\tau),$$

$$\exp(-\alpha_2\tau)\cos(\omega_2\tau), \quad \exp(-\alpha_2\tau)\sin(\omega_2\tau),$$

where

$$\alpha_{1,2}(\mathbf{r}) = \frac{1}{2} \times \times \left(\nu_e \mp \sqrt{\frac{1}{2}\sqrt{\left(\nu_e^2 - \omega_{ce}^2 - 4\omega_{pe}^2\right)^2 + 4\nu_e^2\omega_{ce}^2} + \left(\nu_e^2 - \omega_{ce}^2 - 4\omega_{pe}^2\right)} \right),$$

$$\omega_{1,2}(\mathbf{r}) = \frac{1}{2} \times \times \left(\omega_{ce} \mp \sqrt{\frac{1}{2}\sqrt{\left(\nu_e^2 - \omega_{ce}^2 - 4\omega_{pe}^2\right)^2 + 4\nu_e^2\omega_{ce}^2} - \left(\nu_e^2 - \omega_{ce}^2 - 4\omega_{pe}^2\right)} \right).$$

In the experiments considered, even at a waveguide segment far from the source, waves do not propagate strictly parallel to the Earth surface, but at a small angle relative to the horizon. The magnetic field is also directed at a small angle relative to the vertical to the Earth surface, so the main part for the electric field and for the current is their longitudinal part. This configuration of the fields approximately corresponds to that existing in the high-latitude region of the Earth–ionosphere waveguide for VLF signals from a remote source, and allows us to analyze the processes occurring during signal reflection from the ionosphere.

It follows from the above solution that there are regions with different attenuation patterns of the main longitudinal part of the signal and the vertical position of the boundary between them depends on the ratio of electron collision frequency to plasma frequency.

The dependence of signal attenuation on its frequency obtained for a horizontally homogeneous ionosphere can be explained by the behavior of the $q(z)$ function, whose vertical profile is shown by the red dashed line in panels *a* of Figures 3–5, as well as in panels *a* and *c* of Figures 6 and 7. In the same panels, the black line indicates the electric field strength vertical component modulus averaged over space at a distance of 100 km along the wave normal $\langle |E_z| \rangle_{100\text{ км}}(z)$. This profile represents the height of signal reflection and characteristic signal electric field values in the waveguide at altitudes from 0 to 80 km.

In panels *b* of Figures 3–5, the red line shows the vertical profile of the frequency of collisions of electrons with neutral atoms and ions $\nu_e(z)$; the blue line, the vertical profile of the doubled plasma frequency $2\omega_{pe}(z)$. The intersection point of these plots, marked with a circle in panels *a* and *b*, z_0, such that $\nu_e(z_0) = 2\omega_{pe}(z_0)$ and $q(z_0) = 0$, defines the boundary between regions with different signal attenuation patterns. The derivatives of function $q(z) = \sqrt{\left|\nu_e^2(z) - 4\omega_{pe}^2(z)\right|}$ from below and from above at this point are seen to be close to infinities of different signs.

The panels *c* in Figures 3–5 illustrate vertical distributions of the electric field strength (E_z-component) modulus, which can be used to determine RSDN-20 signal reflection heights.

Analysis of Figures 3–5 shows that under quiet conditions the point z_0, where $\nu_e(z_0) = 2\omega_{pe}(z_0)$ and $q(z_0) = 0$, is in the lower part of the region of signal reflection from the ionosphere (see Figure 3). Under conditions of electron density enhancement of moderate intensity during the arrival of GLE PC, this point z_0 appears to be inside the signal reflection region (see Figure 4), and during the arrival of GLE DC when the density increase was significant, the RSDN-20 signal reflection height decreased so much that z_0 was found to be higher than the reflection region (Figure 5).

In Figures 6, 7 in panels *a* and *c*, the red dashed line indicates the vertical profile of the function $q(z)$; the black line, the vertical profile of the electric field strength vertical component modulus averaged over space at a distance of 100 km along the wave normal $\langle |E_z| \rangle_{100\text{ км}}(z)$. Panels *b* and *d* present vertical distributions of the electric field strength (E_z-component) modulus.

In Figure 6, for the parameters of the ionosphere over Apatity both under quiet conditions (panels *a* and *b*) and in conditions with GLE (panels *c* and *d*), the point z_0, such that the function $q(z_0)=0$, appears to be inside the signal reflection region. In Figure 7, for the parameters of the ionosphere over Barentsburg under quiet conditions (panels *a* and *b*), the point z_0 of the vanishing $q(z)$ function is located inside the signal reflection region, and under conditions with GLE (panels *c* and *d*), z_0 is on the upper boundary of the signal reflection region.

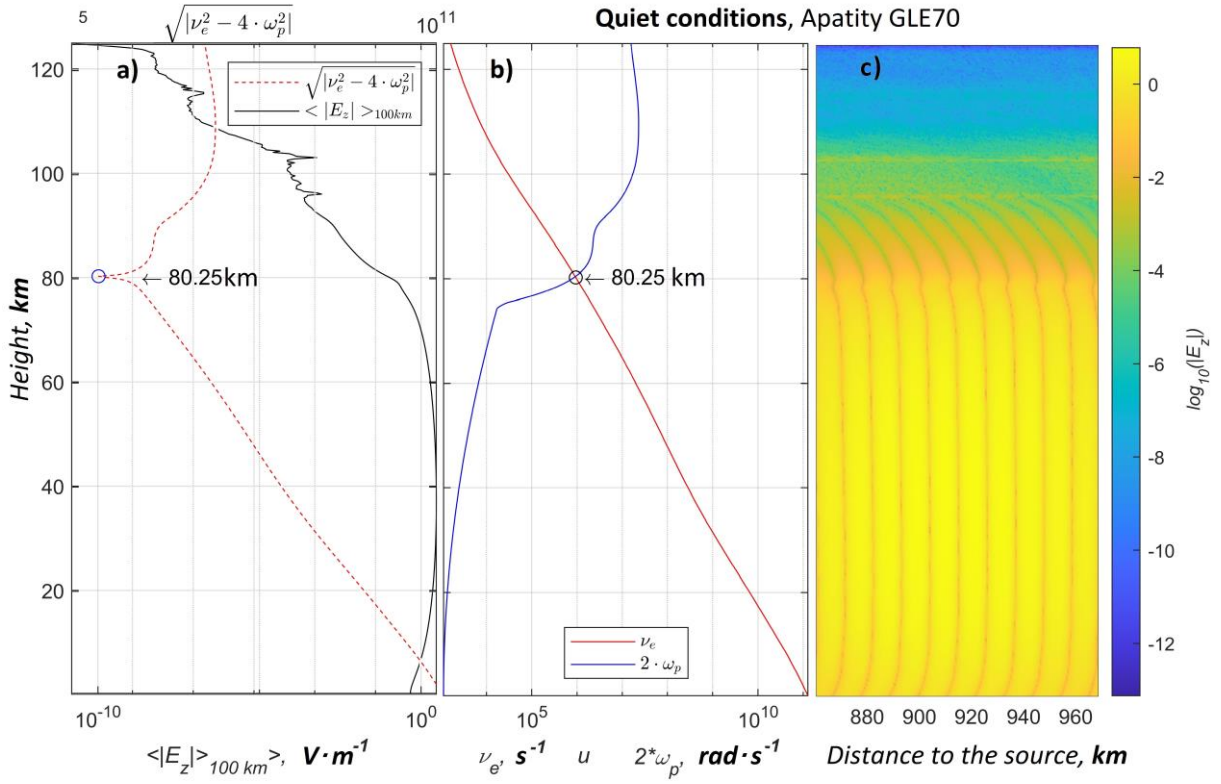

Figure 3. Results of calculations for quiet conditions without regard to ionization by high-energy protons during GLE70 with parameters of the ionosphere over Apatity. Panel *a*: the red dashed line is the *q*(*z*) function; the black line is the electric field strength vertical component modulus averaged over space at a distance of 100 km along the wave normal $\langle |E_z| \rangle_{100\text{ км}}(z)$. Panel *b*: the red line is the electron collision frequency profile $\nu_e(z)$; the blue line is the doubled plasma frequency $2\omega_{pe}(z)$. Panel *c*: vertical distribution of the electric field strength (E_z-component) modulus

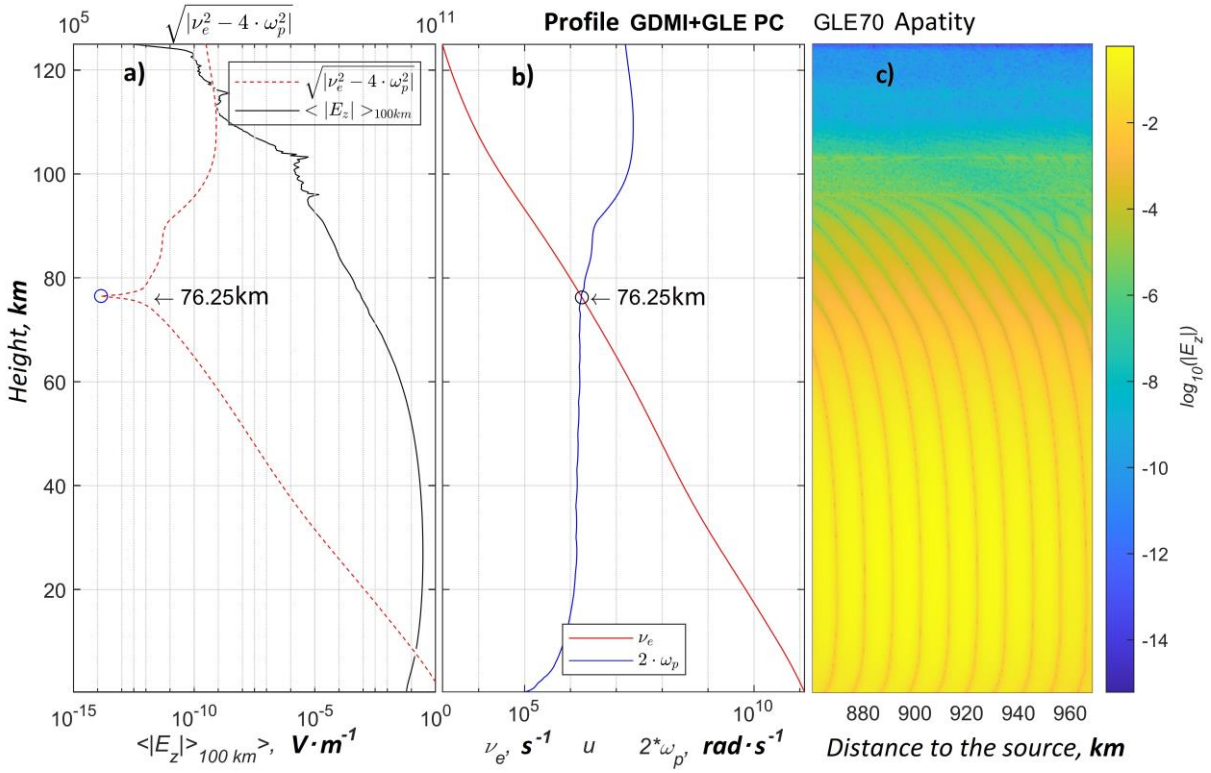

Figure 4. Results of calculation for disturbed conditions with regard to ionization by high-energy protons during GLE70 (PC) with parameters of the ionosphere over Apatity. Designations are the same as in Figure 3

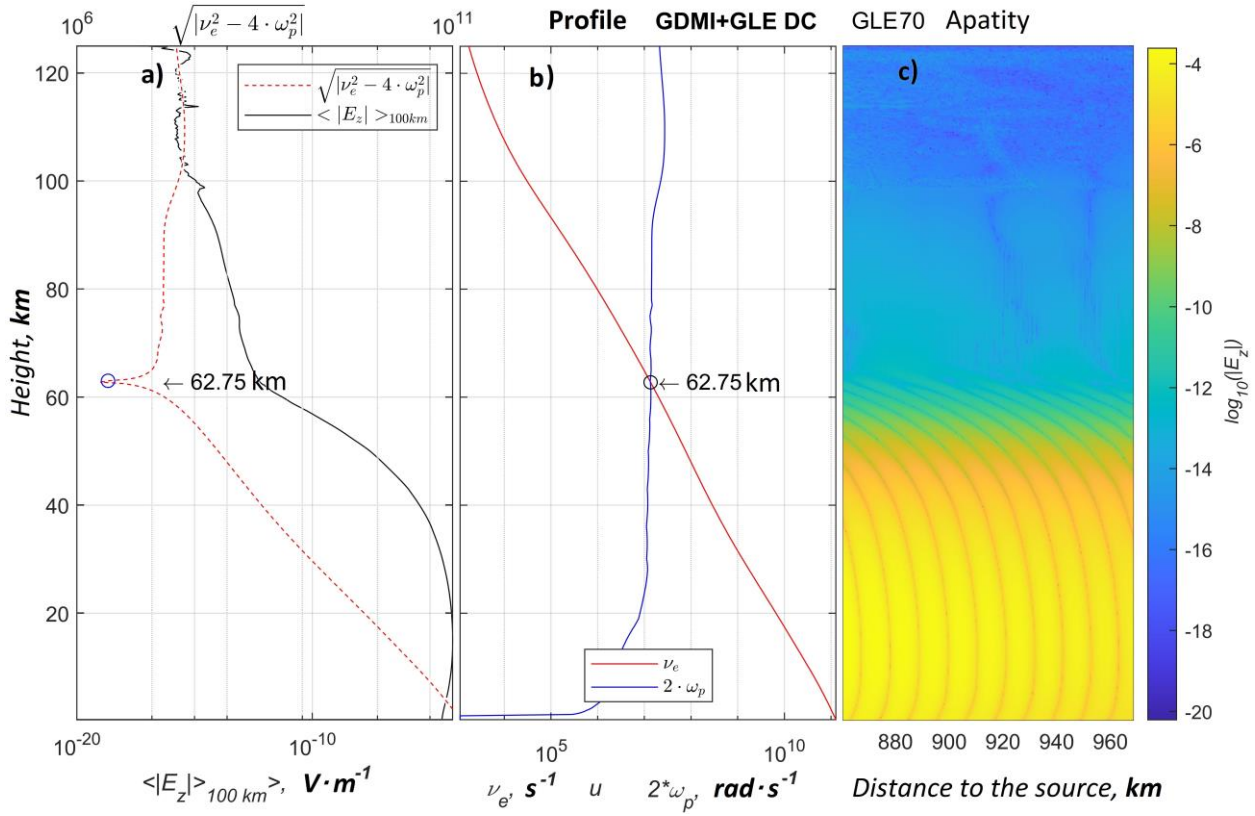

Figure 5. The same as in Figure 4 during the arrival of GLE70 DC

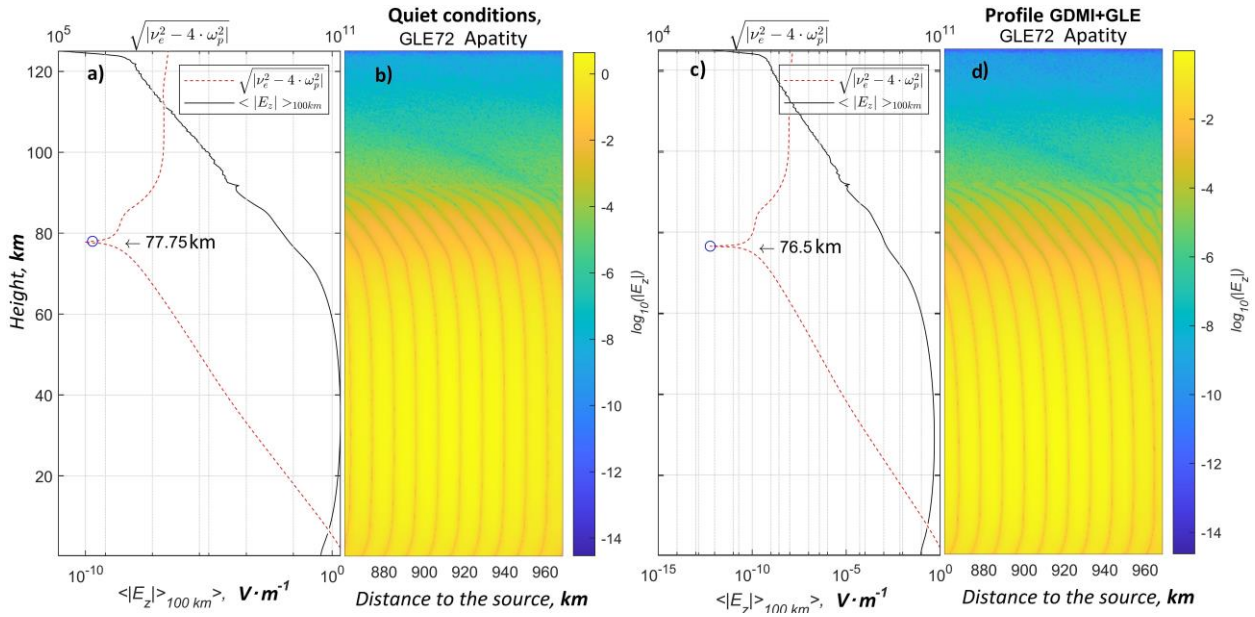

Figure 6. Calculation results for GLE72 with parameters of the ionosphere over Apatity. Panels *a*, *c*: the red dashed line is the *q*(*z*) function; the black line is the electric field strength vertical component modulus averaged over space at a distance of 100 km along the wave normal $\left\langle \left| E_z \right| \right\rangle_{100\text{ км}} (z)$. Panels *b*, *d*: vertical distribution of the electric field strength (E_z-component) modulus. Panels *a*, *b* present the results for quiet conditions without regard to additional ionization; panels *c*, *d*, with regard to additional ionization by high-energy protons during GLE72

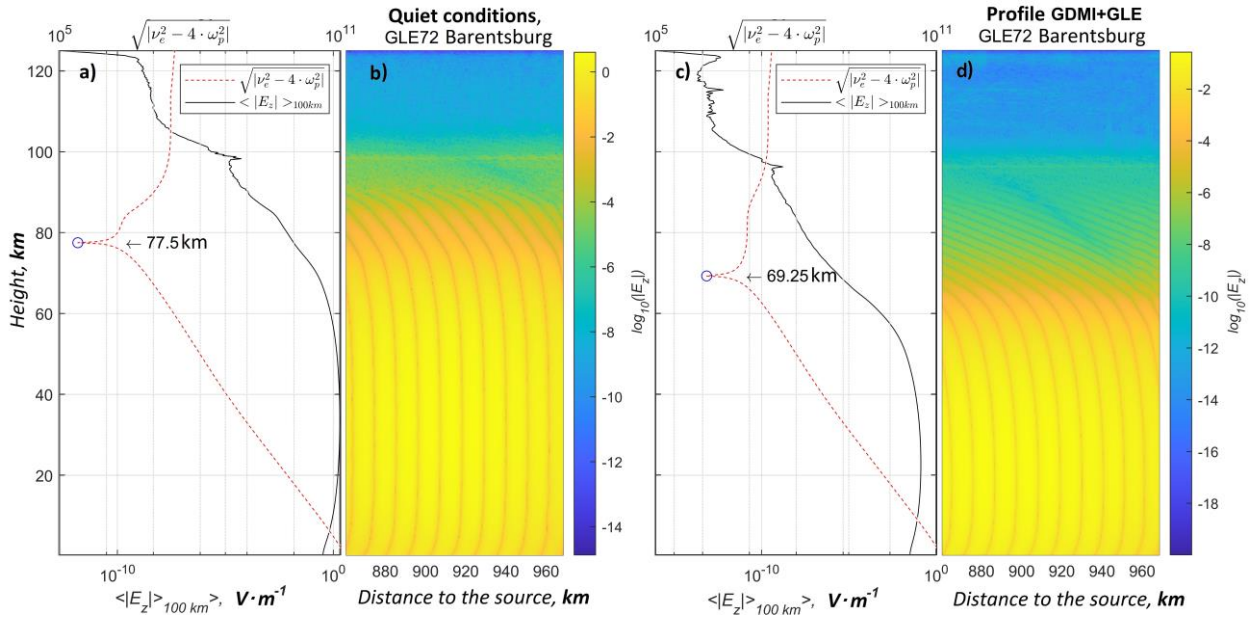

Figure 7. The same as in Figure 6 for parameters of the ionosphere over Barentsburg

Comparing the relative position of z_0 of the vanishing $q(z)$ function and the RSDN-20 signal reflection region (see Figures 3–7) with the plots of Pointing vector attenuation as a percentage per 1 km of radio paths as function of frequency (see Figure 2), we can conclude that the attenuation dependence on frequency is related to the position of z_0. When z_0 is inside the signal reflection region, the attenuation dependence on frequency is nonlinear. When z_0 is above the signal reflection region, the attenuation dependence on frequency tends to linear, and then signals at low frequencies attenuate more rapidly than signals at high frequencies

5. ANALYSIS OF MEASUREMENTS AT OBSERVATORIES

Figure 8 plots daily neutron monitor count rate as a percentage of the average value on September 10, 2017. We have used 5-min averaging for the data. There is a noticeable increase in the neutron count rate after 16 UT. Analysis of ground-based data from Lovozero and Tuloma observatories on September 10, 2017 from 16:00 to 16:40 UT has revealed a marked decrease in the amplitude of RSDN-20 signals at all frequencies. Figure 9 presents the amplitudes of the magnetic field strength of a signal from the Krasnodar transmitter, which were recorded at Lovozero (68°02' N 35°00' E) and Tuloma (68°49' N 32°42' E) observatories on September 10, 2017 during GLE72.

Figure 9, *a*, *b* depicts a decrease in signal amplitudes at all frequencies considered at Lovozero and Tuloma observatories. Note that the signal at a frequency of 14881 Hz during GLE attenuates more rapidly than signals at frequencies of 11905 and 12649 Hz, which attenuate almost equally. This is attributed to the small difference (less than 1 kHz) between their frequencies.

The results of observations at Lovozero and Tuloma observatories during GLE72 are generally consistent with those of the computational experiment. Signal amplitudes decrease at all RSDN-20 frequencies, as well as in the computational experiment. At the same time, there are differences: in the computational experiment, the signal at a frequency of 14881 Hz during GLE attenuates more slowly than the signals at frequencies of 11905 and 12649 Hz, whereas in the results of observations the opposite is true (see Table 1 and Figure 9). The amplitude attenuation in the computational experiment is more rapid.

At midlatitudes, according to the data from the Geophysical Observatory Mikhnevo (54.9° N, 37.8° E) of the Institute of Geosphere Dynamics of the Russian Academy of Sciences, on the contrary, an increase was recorded in the amplitude of VLF signals from transmitters GQD (22100 Hz, 54.732° N, 2.883° E) and GBZ (19580 Hz, 54.912° N, 3.278° E), located in the UK [Gavrilov et al., 2019].

6. DISCUSSION

We should point out limitations of the methods used in this work. The results of computational experiments using the numerical model of electromagnetic wave propagation depend on a given signal source and conditions of propagation media, which is both an advantage of this method and its main disadvantage.

Errors in specifying the source occur due to a mismatch between the given field configuration and the current conditions of the propagation medium. Ideally matching the source with the medium and the model system of equations is an enormous challenge, especially if the source is not point, but the effect of this mismatch on the results decreases rapidly with increasing distance to the source. In this paper, we analyze the results of computational experiments for the most remote part of the rectangular modeling region at a distance of 850 km from the source.

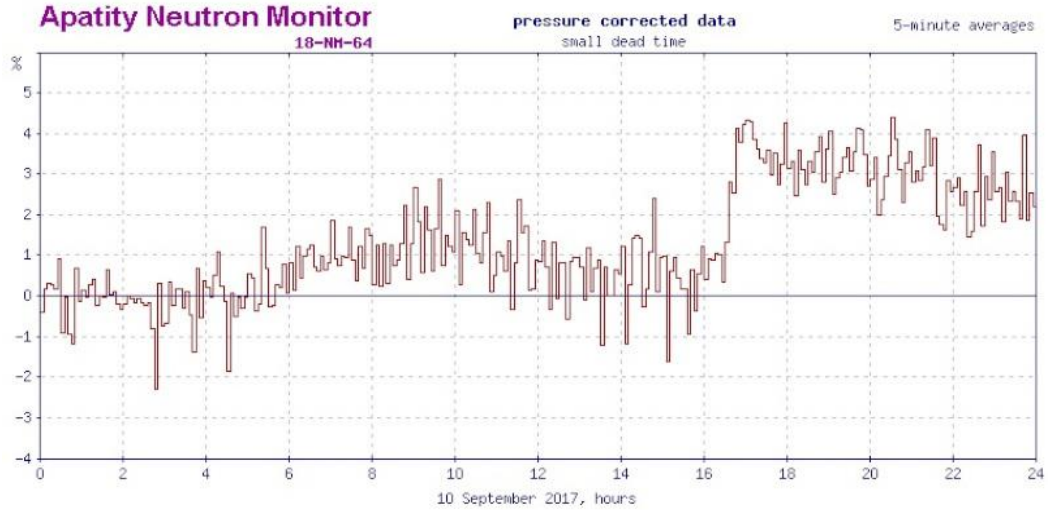

Figure 8. Neutron monitor count rate as a percentage of the average on September 10, 2017. We apply 5-min averaging to the data; along the X-axis is UT

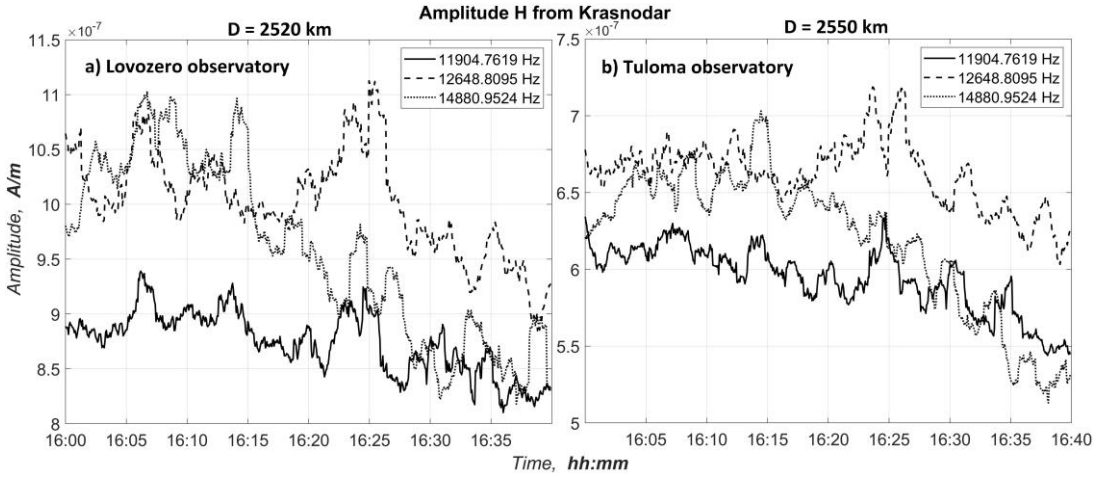

Figure 9. Amplitudes of the magnetic field strength of a signal from a Krasnodar transmitter, which were recorded on September 10, 2017: *a* — at Lovozero Observatory; *b* — at Tuloma Observatory; along the X-axis is UT

Unlike an imperfectly defined source, inaccurately defined conditions of propagation media cannot be compensated in any way. It should, however, be borne in mind that there are regions of propagation media whose effect on the computational experiment results is weak. For example, the lithosphere structure has little effect on signals of the frequency range considered. The waveguide segments with a low electron density or a high frequency of collisions of electrons with neutral particles and ions, which include the troposphere under any conditions and the lower atmosphere up to 50–60 km under quiet conditions, have almost no effect on the signal either. The signal reflection region, on the contrary, is of particular concern, and small deviations in a given electron density profile can have a noticeable effect on signal attenuation. Despite the general trend to decrease the signal amplitude observed by both Lovozero and Tuloma observatories and the computational experiment, noticeable differences were seen between the simulated and recorded behavior of signals of different frequencies during GLE72. So in the computational experiment, a signal at a frequency of 14881 Hz during GLE attenuated more slowly than signals at frequencies of 11905 and 12649 Hz; and in the results of observations the opposite is true (see Table 1 and Figure 9). The reasons for this discrepancy between the results may be an incomplete correspondence between the model electron density profile and the real profile in the signal reflection region, the presence of a strongly horizontally inhomogeneous ionosphere [Akhmetov et al., 2023], or both.

Possible inaccuracies in setting ionospheric parameters do not make the results of computational experiments incorrect since they fully correspond to the electron density profiles presented in Figure 1, yet the profiles per se may not fully correspond to the real conditions that existed during GLE72 on September 10, 2017. Unfortunately, it is not possible to perform systematic measurements of electron density and temperature in the altitude range from 1 to ~70 km; at high altitudes, they are very expensive, which makes the network of radars and ionosondes extremely rare. In such conditions, there is often no alternative to model electron density profiles.

For monitoring of ionospheric conditions on high-latitude radio paths, RSDN-20 signals can be used if the distance between measurement points is sufficiently small (~200 km) and their significant distance from the signal source is more than 1000 km. The limitation of the radio path length is due to the significant horizontal irregularity of the high-latitude ionosphere, which, as shown in [Akhmetov et al., 2023], leads to noticeable distortions of RSDN-20 signals. The probability of significant irregularities along a short radio path is less than along a long one. The requirement for the distance from the source is imposed by the interference overlap of multiple signal modes in near and middle zones, which hampers the interpretation of the results. Thus, only the Krasnodar RSDN-20 transmitter (45°24' N 38°09' E), whose signal goes almost strictly from south to north, is well suited for ionospheric studies on the Kola Peninsula. Signals from other transmitters go rather from east to west; and before they are recorded by the PGI observatories, they pass a long section of the radio path at high latitudes

CONCLUSION

In this paper, we have explored the features of RSDN-20 signal propagation in a high-latitude region of the Earth–ionosphere waveguide during the GLE70 and GLE72 events, using numerical simulation. From joint analysis of part of Maxwell's equations, related to electromagnetic signal attenuation, and the results of computational experiments, we have found a violation of monotonicity in the frequency dependence of signal attenuation. We have shown that this is due to the signal reflection height and the vertical profiles of the electron density and the frequency of collisions of electrons with neutral particles and ions.

We have estimated signal amplitude attenuation and phase delay under quiet conditions and under conditions with GLE events. The estimates can be used for short radio paths 100–200 km in a high- latitude region to monitor ionospheric conditions.

During the strong GLE70 event at the latitude of Apatity, signal attenuation can increase ~6 times; and during the weak GLE72 event, ~2 times. At the latitude of Barentsburg, the attenuation became three times more rapid during GLE72.

We have found that when the intersection point of the vertical electron collision frequency profile $\nu_e(z)$ with the doubled plasma frequency profile $2\omega_{pe}(z)$ is inside a signal reflection region, there is a nonlinear dependence of attenuation on frequency. When the intersection point of these profiles is above a signal reflection region, the frequency dependence of attenuation is close to decreasing linear, and then signals at low frequencies attenuate more rapidly than signals at high frequencies.

The work was financially supported by RSF Grant (Project No. 18-77-10018) (Akhmetov O.I., Belakhovsky V.B., Maurchev E.A., Balabin Yu.V.) [https://rscf.ru/project/18-77-10018 /].

REFERENCES

Akhmetov O.I., Mingalev I.V., Mingalev O.V., Suvorova Z.V., Belakhovsky V.B., Chernyakov S.M. Determination of the characteristics of INCH waves that react most strongly to minor changes in the electron density of the ionosphere at high latitudes. *Solar-Terrestrial Physics*. 2019, vol. 5, no. 4, pp. 81–90. DOI: 10.12737/stp-54201911.

Akhmetov O.I., Mingalev I.V., Mingalev O.V., Belakhovsky V.B., Suvorova Z.V. Propagation of electromagnetic waves in the region of high latitudes at various states of the ionosphere at frequencies of the RSDN-20 (ALPHA) radionavigation system. *Geomagnetism and Aeronomy*. 2021a, vol. 61, no. 3, pp. 376–388. DOI: 10.1134/S0016793221030026.

Akhmetov O.I., Mingalev I.V., Mingalev O.V., Belakhovsky V.B., Suvorova Z.V. Propagation of electromagnetic waves with frequencies of the Beta time signal service through the ionosphere in different states at high latitudes. *Bulletin of the Russian Academy of Sciences: Physics*. 2021b, vol. 85, no. 3, pp. 224–229. DOI: 10.3103/S1062873821020039.

Akhmetov O.I., Belakhovsky V.B., Mingalev I.V., Mingalev O.V., Larchenko A.V., Suvorova Z.V. About the propagation of RSDN-20 “Alpha” signals in the Earth-ionosphere waveguide during geomagnetic disturbances. *Radio Sci.* 2023, vol. 58, e2022RS007490. DOI: 10.1029/2022RS007490.

Alken P., Thébault E., Beggan C.D., Amit H., Aubert J., Baerenzung J., et al. International Geomagnetic Reference Field: the thirteenth generation. *Earth Planets Space.* 2021, vol. 73, 49. DOI: 10.1186/s40623-020-01288-x.

Clilverd M., Seppälä A., Rodger C., Thomson N., Verronen P., Turunen E., et al. Modeling polar ionospheric effects during the October–November 2003 solar proton events. *Radio Sci.* 2006, vol. 41, id RS2001. DOI: 10.1029/2005RS003290.

Deminov M.G., Shubin V.N., Baidin V.I. Model of the E-layer critical frequency for the auroral region. *Geomagnetism and Aeronomy*. 2021, vol. 61, no. 5, pp. 713–720. DOI: 10.1134/S0016793221050054.

Dowden R.L., Adams C.D.D. Phase and amplitude perturbations on the NWC signal at Dunedin from lightning-induced electron precipitation. *J. Geophys. Res.: Space Phys.* 1989, vol. 94, iss. A1, pp. 497–503. DOI: 10.1029/JA094iA01p00497.

Gavrilov B.G., Ermak V.M., Poklad Yu.V., Ryakhovsky I.A. Estimate of variations in the parameters of the midlatitude lower ionosphere caused by the solar flare of September 10, 2017. *Geomagnetism and Aeronomy*. 2019, vol. 59, no. 5, pp. 587–592. DOI: 10.1134/S0016793219050049.

Gledhill J.A. The effective recombination coefficient of electrons in the ionosphere between 50 and 150 km. *Radio Sci.* 1986, vol. 21, no. 3, pp. 399–408. DOI: 10.1029/RS021i003p00399.

Hargreaves J.K. *The upper atmosphere and solar-terrestrial relations: An introduction to the aerospace environment.* 1st edition.Van Nostrand Reinhold, 1979, 298 p.

Inan U.S., Cummer S.A., Marshall R.A. A survey of ELF and VLF research on lightning-ionosphere interactions and causative discharges. *J. Geophys. Res.: Space Phys*. 2010, vol. 115, iss. A6, A00E36. DOI: 10.1029/2009JA014775.

Knipp D., Ramsay A., Beard E., Boright A., Cade T., Hewins I., et al. The May 1967 great storm and radio disruption event: Extreme space weather and extraordinary responses. *Space Weather*. 2016, vol. 14, pp. 614–633. DOI: 10.1002/2016sw001423.

Korja T., Engels M., Zhamaletdinov A.A., Kovtun A.A., Palshin N.A., Smirnov M. Yu., et al. Crustal conductivity in Fennoscandia — a compilation of a database on crustal conductance in the fennoscandian shield. *Earth Planets Space*. 2002, vol. 54, no. 5, pp. 535–558. DOI: 10.1186/BF03353044.

Lifshits E.M., Pitaevsky L.P. *Fizicheskaya kinetika* [Physical Kinetics]. Moscow, Nauka Publ., 1979, 527 p. (Landau L.D., Lifshits E.M. *Teoreticheskaya fizika*. [Theoretical Physics]. Vol. X). (In Russian).

Marshall R.A., Wallace T., Turbe M. Finite-difference modeling of very-low-frequency propagation in the earth-ionosphere waveguide. *IEEE Trans. Antennas Propag*. 2017,

vol. 65, no. 12, pp. 7185–7197. DOI: 10.1109/TAP.2017.2758392.

Maurchev E.A., Balabin Yu.V. Model complex for the study of cosmic rays. *Solar-Terrestrial Physics*. 2016, vol. 2, no. 4, pp. 3–10. DOI: 10.12737/24269.

Meyer P., Parker E.N., Simpson J.A. Solar cosmic rays of February 1956 and their propagation through interplanetary space. *Phys. Rev.* 1956, vol. 104, no. 3, pp. 768–783.

Mishev A., Velinov P.I.Y. Determination of medium time scale ionization effects at various altitudes in the stratosphere and troposphere during ground level enhancement due to solar cosmic rays on 13.12.2006 (GLE 70). *C.R. Acad. Bulg. Sci.* 2015, vol. 68, pp. 1427–1432.

Perez-Peraza J.A., Márquez-Adame J.C., Caballero-Lopez R.A., Manzano I., Roberto R. Spectra of the two official GLEs of solar cycle 24. *Adv. Space Res.* 2020, vol. 65, iss. 1, pp. 663–676. DOI: 10.1016/j.asr.2019.10.021.

Shubin V.N., Krasheninnikov I.V., Merzly A.M., Reznikov A.E., Yanakov A.T., Tikhonov M.V. Dynamic Model of the High-latitude Ionosphere (DMHI): Certificate of the computer program state registration No. 2021616554 Russian Federation. 22.04.2021; applicant *Federal'noe gosudarstvennoe byudzhetnoe uchrezhdenie nauki Institut kosmicheskih issledovanij Rossijskoj akademii nauk* [Federal State Budgetary Institution of Science Institute of Space Research of the Russian Academy of Sciences]. 2021.

Shubin V.N. Global empirical model of critical frequency of the ionospheric F2-layer for quiet geomagnetic conditions. *Geomagnetism and Aeronomy*. 2017, vol. 57, no. 4, pp. 414–425. DOI: 10.1134/S0016793217040181.

Schunk R., Nagy A. *Ionospheres: Physics, Plasma Physics, and Chemistry:* 2nd ed. Cambridge, Cambridge University Press, 2009, 355 p. (Cambridge Atmospheric and Space Science Ser.). DOI: 10.1017/CBO9780511635342.

Wait J.R., Spies K.P. *Characteristics of the Earth-ionosphere waveguide for VLF radio waves*. *Technical Note 300*. Boulder, National Bureau of Standards, 1964, 96 p.

Original Russian version: Akhmetov O.I., Mingalev I.V., Mingalev O.V., Belakhovsky V.B., Maurchev E.A., Larchenko A.V., Suvorova Z.V., Balabin Yu.V., published in Solnechno-zemnaya fizika. 2023. Vol. 9. Iss. 3. P. 41–51. DOI: 10.12737/szf-93202305.

How to cite this article

Akhmetov O.I., Mingalev I.V., Mingalev O.V., Belakhovsky V.B., Maurchev E.A., Larchenko A.V., Suvorova Z.V., Balabin Yu.V. Influence of strong solar proton events on propagation of radio signals in the VLF range in a high-latitude region. *Solar-Terrestrial Physics*. 2023. Vol. 9. Iss. 3. P. 30–42. DOI: 10.12737/stp-93202305.